Journal of Photochemistry and Photobiology A: Chemistry 221 (2011) 123–127

Contents lists available at ScienceDirect

Journal of Photochemistry and Photobiology A: Chemistry

journal homepage: www.elsevier.com/locate/jphotochem

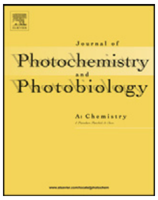

Photodissociation dynamics of Cl_2O at 235 nm using velocity map ion imaging

Hahkjoon Kim[a,*], Simon W. North[b]

[a] Department of Chemistry, Duksung Women's University, 419 SSangmundong, Seoul, Republic of Korea
[b] Department of Chemistry, Texas A&M University, P.O. Box 30012, College Station, TX 77842, United States

ARTICLE INFO

Article history:
Received 22 February 2011
Received in revised form 16 April 2011
Accepted 22 April 2011
Available online 30 April 2011

Keywords:
Chlorine monoxide
Velocity map ion imaging
REMPI
Secondary photodissociation
Speed-dependent anisotropy

ABSTRACT

We have investigated the photodissociation dynamics of expansion-cooled Cl_2O at 235 nm using photofragment velocity map ion imaging coupled with resonance-enhanced multiphoton ionization (REMPI) to measure the speed and angular distributions of the $Cl(^2P_{3/2})$ and $Cl(^2P_{1/2})$ products. We observe speed-dependent spatial anisotropy for both Cl fragments from the imaging data and attribute this to a fraction of nascent ClO, which undergoes secondary photodissociation. We have employed a Monte–Carlo forward-convolution scheme to analyze the data and obtain the speed distribution and anisotropy parameters for the $ClO + Cl(^2P_{3/2,1/2})$ channels. We find that the speed distribution of the $Cl(^2P_{3/2}) + ClO$ channel is bimodal with an anisotropy parameter of 1.2 ± 0.2, whereas the speed distribution of the $Cl(^2P_{1/2}) + ClO$ channel consists of a single component with an anisotropy parameter of 1.0 ± 0.2. We have determined branching ratios for $Cl(^2P_{3/2}) + ClO$ and $Cl(^2P_{1/2}) + ClO$ channels to be $0.97 \pm 0.02{:}0.03 \pm 0.02$. Based on the translational energy distribution of $Cl(^2P_{3/2}) + ClO$ channel, 28% of the parent molecule undergoes three-body dissociation.

1. Introduction

The photochemistry of chlorine-containing species has received considerable attention due to their role in the catalytic destruction of ozone in the stratosphere [1,2]. Although Cl_2O (chlorine monoxide) is known to be a minor agent in stratospheric ozone destruction, it is an anhydride form of HOCl, which is one of the major chlorine oxides in the atmosphere. In addition, since Cl_2O is frequently used as a precursor to important chlorine-oxides such as ClO and $ClONO_2$ in the laboratory [3,4], it is necessary to characterize the photodissociation dynamics of Cl_2O to permit analysis of the ClO and $ClONO_2$ data. In the field of reaction dynamics, it is an ideal molecule for the study for three-body dissociation dynamics [5–7]. The absorption spectrum of Cl_2O exhibits overlapping broad bands with distinguished features at 410, 285, 256, and 171 nm [8–10]. There have been several theoretical studies to model the absorption spectrum by calculating vertical excitation energies and oscillator strengths of the electronic transitions [11,12]. Nickolaisen et al. have employed the CASSCF/MRSD-DI method to calculate the vertical excitation energies and oscillator strength of various excited states in order to interpret the experimental spectrum [11]. Persico et al. have carried out perturbed MRCI calculations and semiclassical simulations of the excited states to interpret the absorption spectrum and photodissociation dynamics such as bimodal translational energy distributions and anisotropy parameters [12]. Despite differences between theoretical calculations in the interpretation of the absorption spectrum, there is a consensus that the $1\,^1B_2 \leftarrow 1\,^1A_1$ transition is dominant for spectral features between 225 and 325 nm. There have also been several experimental studies of Cl_2O photodissociation [13–16]. There are three dissociation pathways that are energetically accessible in the UV region:

$$Cl_2O + h\nu \rightarrow ClO + Cl(^2P_J) \tag{1}$$

$$Cl_2O + h\nu \rightarrow 2Cl(^2P_J) + O(^3P_J, ^1D) \tag{2}$$

$$Cl_2O + h\nu \rightarrow Cl_2 + O(^3P_J, ^1D) \tag{3}$$

Nelson et al. studied the photodissociation of jet-cooled Cl_2O using photofragment translational spectroscopy (PTS) at 193, 248, and 308 nm and concluded that (1) is the only available channel at 308 nm, a dominant channel at 248 nm and (3) is a dominant channel at 193 nm [13]. The authors also observed bimodal translational energy distributions for the channel (1) at 248 and 308 nm which they attributed to dissociation on different potential energy surfaces. Later, Moore et al. reinvestigated the TOF data and derived three different translational energy components and anisotropy parameters at 248 and 308 nm on the basis of the forward-convolution fittings [14]. Tanaka et al. studied the photodissociation of Cl_2O at 235 nm using photofragment ion imaging coupled with the resonance-enhanced multiphoton ionization (REMPI) technique in order to obtain the speed and angular distributions of $Cl(^2P_{3/2})$ and $Cl(^2P_{1/2})$ [15]. They found that the translational energy distribution of $Cl(^2P_{3/2})$ is significantly differ-

---

[*] Corresponding author. Tel.: +82 2 901 8359; fax: +82 2 901 8351.
E-mail addresses: khj730516@ds.ac.kr, khj730516@duksung.ac.kr (H. Kim).

1010-6030/$ – see front matter © 2011 Elsevier B.V. All rights reserved.
doi:10.1016/j.jphotochem.2011.04.036

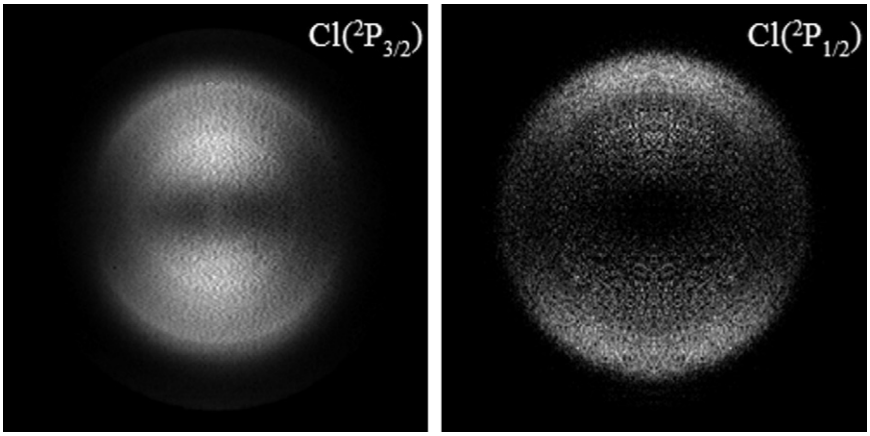

Fig. 1. Raw images of $Cl(^2P_{3/2})$ and $Cl(^2P_{1/2})$ arising from Cl_2O photodissociation at 235 nm.

ent from that of $Cl(^2P_{1/2})$, although the anisotropy parameters of both Cl photofragments were equivalent ($\beta = 1.2 \pm 0.2$). The authors observed no discernible speed-dependent anisotropy parameter, which is in contrast to the results of Moore et al. Recently, Roth et al. investigated the photodissociation of Cl_2O at 235 and 207 nm by using time-of-flight (TOF) REMPI [5,6]. The authors observed bimodal translational energy distributions for both Cl photofragments with an anisotropy parameter of 0.7 ± 0.2 at 235 nm, lower than previously reported. At 207 nm, $Cl(^2P_{3/2})$ and $Cl(^2P_{1/2})$ products were observed with similar translational energy distributions and an anisotropy parameter of 0.2 ± 0.2. From the observed kinetic energy distribution, they concluded that three-body dissociation is significant at both wavelengths. Zou et al. studied the three-body dissociation of Cl_2O at 248 and 193 nm using photofragment translational spectroscopy with tunable VUV photoionization detection [7]. On the basis of the forward-convolution fittings of the TOF spectra, the authors concluded that two there were three-body processes originating from both symmetric stretching and antisymmetric stretching motions in the Franck–Condon region giving rise to bimodal translational energy distributions.

In the present study, we have investigated the photodissociation of expansion-cooled Cl_2O at 235 nm using velocity map ion imaging in combination with the resonance-enhanced multiphoton ionization technique. We have employed Monte–Carlo forward-convolution fitting [17] to model the secondary photodissociation and compare to the experimental data. On the basis of the forward-convolution fits, we find that branching ratios for $Cl(^2P_{3/2}) + ClO$ and $Cl(^2P_{1/2}) + ClO$ channels to be $0.97 \pm 0.02{:}0.03 \pm 0.02$ with anisotropy parameters of $\beta = 1.2 \pm 0.2$ and 1.2 ± 0.4, respectively. We also determined the fraction of three-body dissociation based on the translational energy distribution of both Cl fragments.

2. Experimental

Details of the experimental apparatus are published elsewhere [18,19]. In brief, a pulsed Cl_2O molecular beam, collimated by a conical skimmer, was intersected at 90° by a linearly polarized laser beam. The 235 nm beam was generated using a Nd:YAG (Spectra Physics GCR-150-10) pumped dye laser (LAS LDL 2051) followed by a frequency doubling crystal (BBO). The fundamental wavelength was accurately calibrated using a Ne-filled hollow cathode lamp. The $Cl(^2P_{3/2})$ and $Cl(^2P_{1/2})$ products were probed using 2 + 1 REMPI transitions at 235.336 nm ($4p\,^2D_{3/2} \leftarrow 3p\,^2P_{3/2}$) and 235.205 nm ($4p\,^2P_{1/2} \leftarrow 3p\,^2P_{1/2}$), respectively [20]. The resulting chlorine ions were accelerated by velocity mapping ion optics [21,22] before entering the 50 cm long field-free flight tube along to the axis defined by the molecular beam. The ions were projected on a position-sensitive detector consisting of a dual microchannel plate-phosphor assembly. A photomultiplier (PMT) positioned off-axis was used to record mass spectra and establish proper timing. Images were acquired using a CCD camera and a frame grabber controlled by commercial software (Coda32) which involved centroiding and event counting [23]. The final images were obtained by repeatedly scanning Doppler profiles of the REMPI transitions to achieve homogeneous detection efficiency. The 3-dimensional velocity distributions were reconstructed from the two-dimensional projections using the basis set expansion (BASEX) algorithm developed by Reisler and co-workers [24]. The speed distributions were calibrated by measuring Cl fragments arising from the 235 nm dissociation of ICl [25].

Cl_2O was synthesized by the method of Cady [26]. Cl_2 is collected directly from a lecture bottle without further purification then collected on pre-baked HgO (Aldrich) powder and the reaction was allowed to run overnight at 195 K. The product was then purified by vacuum distillation, and the purity (>90%) was checked by UV absorption spectroscopy.

3. Results and discussion

Fig. 1 shows the raw images of $Cl(^2P_{3/2})$ and $Cl(^2P_{1/2})$ fragments arising from the photodissociation of Cl_2O at 235 nm. The $Cl(^2P_{1/2})$ image (right panel) is qualitatively different from the image reported in the previous study by Tanaka et al. In particular, we observe a significantly lower contribution from slow fragments. Although we did observe slow fragments in some of the measured $Cl(^2P_{1/2})$ images, the signal remained when the probe laser wavelength was detuned from the 2 + 1 REMPI resonance (Supporting Information). Subtraction of the non-resonant signal results in images consistent with the image shown in Fig. 1. On the basis of the image intensity and the relative detection efficiency of $Cl(^2P_{3/2})$ and $Cl(^2P_{1/2})$ [27,28], we determine a $Cl(^2P_{3/2})/Cl(^2P_{1/2})$ branching ratio of 16 ± 2, consistent with, but higher than, the ratio of 13 ± 2 obtained by Tanaka et al. It should be noted that we have used the most recent reported value for the relative detection efficiency for $Cl(^2P_{3/2})/Cl(^2P_{1/2})$ (0.6) based on the work of Wittig and co-workers, while a value of 0.85 was employed in the earlier work of Tanaka et al. Fig. 2 shows the corresponding center-of-mass translational energy distributions of $Cl(^2P_{3/2})$ and $Cl(^2P_{1/2})$ derived from the images in Fig. 1. The translational energy distribution of $Cl(^2P_{3/2})$ exhibits two distinctive peaks located near 35 and 90 kJ/mol, and long tail extending to 220 kJ/mol, consistent with previous studies. These two peaks correspond primarily to three-body dissociation and two-body dissociation. The threshold energies for the three-body dissociation are represented by the vertical dashed lines in Fig. 2. The ratio of the three-body dissocia-

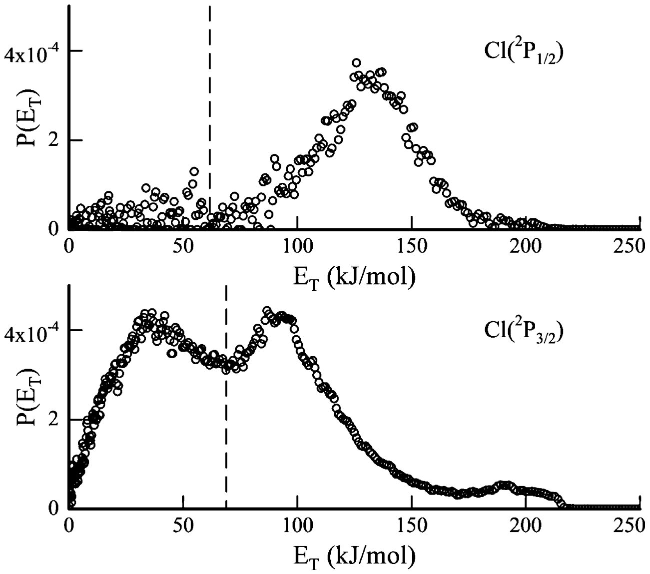

Fig. 2. Translational energy distributions derived from Cl($^2P_{1/2}$) (upper panel) and Cl($^2P_{3/2}$) (lower panel) images in Fig. 1. Vertical lines represent the three-body dissociation threshold.

tion relative to the two-body dissociation can be determined from the forward convolution fits discussed below. A fraction of the stable ClO fragments, associated with the two-body dissociation, can undergo secondary photodissociation (vide infra). The translational energy distribution of Cl($^2P_{1/2}$) fragments is qualitatively different from that of Cl($^2P_{3/2}$), exhibiting a single peak at ~130 kJ/mol with a long tail extending to 220 kJ/mol. The average translational energy of Cl($^2P_{3/2}$) and Cl($^2P_{1/2}$) is 60.7 kJ/mol and 121 kJ/mol, respectively. We speculate that contributions from Cl_2 impurities are insignificant because a sharp feature at 127 kJ/mol, arising from the Cl_2 photodissociation, is not apparent in the translational energy distributions. Fig. 3 shows the angular distributions of the Cl($^2P_{3/2}$) fragments arising from the Cl_2O photodissociation at 235 nm with the translational energy near 50 kJ/mol (bottom) and 200 kJ/mol (top). It is clear that the angular distribution for the slow Cl($^2P_{3/2}$) products is consistent with a $\cos^2\theta$ dependence whereas that for the fastest Cl($^2P_{3/2}$) products is not. We have, therefore, included a $\cos^4\theta$ term in order to fit the data using the following form [29]:

$$P(\theta) \propto \{1 + \beta_2(v) \times P_2(\cos\theta) + \beta_4(v) \times P_4(\cos\theta)\} \tag{4}$$

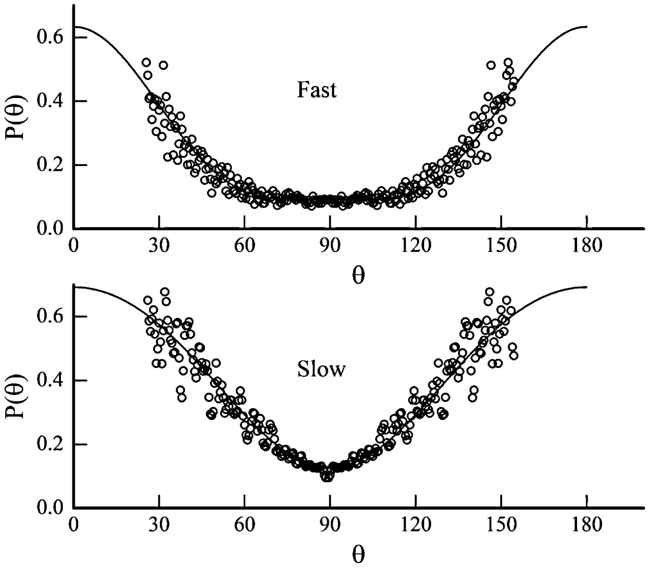

Fig. 3. Angular distributions of Cl($^2P_{3/2}$) in Fig. 1 with the translational energy near 50 and 200 kJ/mol. The solid line is the best-fit simulation obtained using Eq. (4) in the text.

where θ is the recoil angle relative to the electric vector of the dissociating light, $P_2(\cos\theta)$ and $P_4(\cos\theta)$ are the second- and fourth-order Legendre polynomials. We find that values of β_2 and β_4 are 1.5 ± 0.1 and 0.7 ± 0.1, respectively, provide a reasonable fit to the data shown in the lower panel of Fig. 3. Given the previous results that the angular distributions in photodissociation steps (1) and (2) are described by a second-Legendre polynomial, the inclusion of the fourth-Legendre polynomial suggests that a fraction of Cl($^2P_{3/2}$) fragments in the image arise from the secondary photodissociation of ClO by the tightly focused laser [17]. It is important to note that the observation of the fourth-Legendre contribution to the angular distribution can also arise from an atomic orbital alignment of the chlorine atoms although this effect is not considered in this paper. Previous studies of Cl + ClO photodissociation using 2 + 1 REMPI detection of the Cl fragments did not report a fourth-Legendre contribution to the angular distribution [5,6,15]. Details of modeling secondary photodissociation and spontaneous secondary dissociation are discussed in our previous publication on the $ClONO_2$ system [17]. In brief, when secondary photodissociation occurs the final angular distribution of the fragments will be a product of each dissociation step:

$$P_1(\cos\theta) \times P_2(\cos\theta) = \left\{1 + \beta_1 \times \left(\frac{3\cos^2\theta - 1}{2}\right)\right\} \times \left\{1 + \beta_2 \times \left(\frac{3\cos^2\theta - 1}{2}\right)\right\} \tag{5}$$

resulting in a $\cos^4\theta$ term in the angular distribution. In contrast, for three-body dissociation, where spontaneous secondary dissociation of a triatomic occurs within a vibrational period of the intermediate, the final angular distribution will depend on only $P_2(\cos\theta)$. The primary dissociation channel produces Cl($^2P_{3/2}$) and Cl($^2P_{1/2}$) via the following pathways:

$$Cl_2O + h\nu \rightarrow ClO + Cl(^2P_{3/2}) \tag{1a}$$

$$\rightarrow ClO + Cl(^2P_{1/2}) \tag{1b}$$

The branching ratio of (1a)/(1b) is expected to be large on the basis of the image intensity and can be obtained by the combination of the image intensity and forward-convolution fits. The photodissociation of ClO at 235 nm has been studied previously [30] revealing that the dominant channel is Cl($^2P_{3/2}$) + O($^1D_2$) with a relative yield of >0.98 and an anisotropy parameter of β = 1.8 ± 0.2. One of the important minor channels was Cl($^2P_{1/2}$) + O($^1D_2$) with an anisotropy parameter of β = −1 ± 0.1. On the basis of the branching ratios of the overall dissociation pathways, the Cl($^2P_{3/2,}$) image has contributions from the primary dissociation, three-body dissociation and secondary photodissociation, whereas the Cl($^2P_{1/2}$) image has contributions limited to the primary dissociation and secondary photodissociation. It should be noted that the branching ratio and anisotropy parameters for the ClO dissociation at 235 nm have been shown to be identical irrespective of the vibrational state at this wavelength [30]. The speed distribution of ClO, $P(v_1)$, arising from the primary dissociation can be established by Monte–Carlo sampling weighted by the following functional form:

$$P(v_1) = a \times \exp\left(\frac{-(v_1 - a_1)^2}{a_2}\right) + b \times \exp\left(\frac{-(v_1 - b_2)^2}{b_2}\right) \tag{6}$$

where parameters in (6) are adjustable and reflect the image data as shown in Fig. 1. The speed-independent angular distribution of ClO is given by:

$$P(\theta) = 1 + \beta_2 \times \left(\frac{3\cos^2\theta_1 - 1}{2}\right) \tag{7}$$

The joint probability associated with the velocity of the ClO fragment is then given by

$$P(\overline{v_1}) = P(v_1) \times P(\theta_1) \tag{8}$$

The internal energy of the ClO fragment can be determined by energy conservation:

$$E_{\mathrm{avail}} = h\nu - D_0^{\mathrm{o}}(\mathrm{Cl{-}ClO}) = E_{\mathrm{trans}} + E_{\mathrm{int}}(\mathrm{ClO}) + E_{\mathrm{int}}(\mathrm{Cl}) \tag{9}$$

where $h\nu$ is the photon energy, $D_0^{\mathrm{o}}(\mathrm{Cl{-}ClO})$ is the bond dissociation energy of Cl_2O, E_{trans} is the total translational energy determined from image data, $E_{\mathrm{int}}(\mathrm{ClO})$ is the internal energy of the ClO fragment, and $E_{\mathrm{int}}(\mathrm{Cl})$ is the internal energy of the Cl fragment. Only stable ClO resulting from the primary dissociation is expected to undergo secondary photodissociation. The energy available for translation of the Cl atom upon secondary photodissociation includes the internal energy of the ClO

$$E_T = h\nu - D_0^{\mathrm{o}}(\mathrm{Cl{-}O}) + E_{\mathrm{int}}(\mathrm{ClO}) - E_{\mathrm{int}}(\mathrm{O}) \tag{10}$$

where $D_0^{\mathrm{o}}(\mathrm{Cl{-}O})$ is the bond dissociation energy of ClO (38050 cm^{-1}) and $E_{\mathrm{int}}(\mathrm{O})$ is the internal energy of the O fragment. The speed distribution of the secondary photodissociation can be evaluated using (9), (10) and its angular distribution is described by the same functional from in (7) using the speed-independent anisotropy parameters reported in the previous study. The vector sum of the two dissociation steps provides a resultant vector representing the Cl fragment velocity with respect to the axis of linear polarization of the dissociation laser with a probability equal to the joint probabilities of the individual vectors.

$$P(\overline{v}) = P(\overline{v_1}) \times P(\overline{v_2}) \tag{11}$$

ClO fragments with internal energy in excess of the bond dissociation energy will undergo spontaneous secondary dissociation within a vibrational period. The energy available to the fragments of ClO dissociation can be described by conservation of energy.

$$E_{\mathrm{avail}} = E_{\mathrm{int}}(\mathrm{ClO}) - D_0^{\mathrm{o}}(\mathrm{Cl{-}O}) = E_{\mathrm{trans}} + E_{\mathrm{int}}(\mathrm{Cl}) + E_{\mathrm{int}}(\mathrm{O}) \tag{12}$$

Angular distribution of the spontaneous secondary dissociation was described by a Gaussian (FWHM 20°) function centered at 40° used to fit TOF spectrum of Cl_2O photodissociation at 193 and 248 nm [7]. Fig. 4(a) shows the derived speed distribution of $\mathrm{Cl}(^2\mathrm{P}_{3/2})$ from the primary dissociation of Cl + ClO. A vertical line represents the threshold for spontaneous secondary dissociation and slow components marked by 'I' undergo spontaneous secondary dissociation. A small fraction of the fast components marked by 'II' undergo secondary photodissociation. Fig. 4(b) shows a best-fit speed distribution of Cl fragments (solid line) from the primary dissociation (dashed line), secondary photodissociation (SP: dot and dashed line), spontaneous secondary dissociation (SSD: dotted line), and speed distribution from the image data (circle). It should be mentioned that we have ignored rotational metastability of ClO resulting some degree of disagreement between data and fits. From the previous studies, it is known that a bimodal translational energy distribution is due to a bifurcation of the $^1\mathrm{B}_2$ state along the reaction coordinate resulting in the symmetric (slow ClO) and asymmetric (fast ClO) stretching motion of the parent molecule. Our data show that the fraction of the slow ClO in coincidence with $\mathrm{Cl}(^2\mathrm{P}_{3/2})$ is higher than the 248 nm data by Zou et al., which is in good agreement with previous expectation that the symmetric stretch will increase at shorter wavelength [7]. We find that 28% of the parent molecule undergoes spontaneous secondary dissociation by comparing the speed distributions of the primary distribution and secondary spontaneous dissociation in Fig. 4. The lack of slow $\mathrm{Cl}(^2\mathrm{P}_{1/2})$ products indicates that the dissociation pathways along the potential energy surface for (1a) and (1b) may be considerably different although their initial origin ($^1\mathrm{B}_2$) is identical on the basis of the anisotropy parameters. As Tanaka et al. proposed, the $\mathrm{Cl}(^2\mathrm{P}_{3/2})$ + ClO channel is available through nonadiabatic crossings to relatively low potential energy surfaces from the $^1\mathrm{B}_2$ state that correlates to the $\mathrm{Cl}(^2\mathrm{P}_{1/2})$ + ClO channel [15]. The fraction of secondary photodissociation can be determined by integrating the speed distribution of the primary and secondary photodissociation. This fraction can be increased with laser fluence but may lead to saturation of the primary photodissociation, thereby reducing the original anisotropy parameter. From the image intensity data along with the fraction of the secondary dissociation, we have determined branching ratios for the 1(a) and 1(b) channels to be 0.97 ± 0.02: 0.03 ± 0.02. Bottom panel in Fig. 5 shows the derived β_2 of the $\mathrm{Cl}(^2\mathrm{P}_{3/2})$ fragments (circle) from the image data along with the Monte–Carlo forward-convolution fits using the anisotropy parameters for the primary dissociation of 1.2 averaged over a 250-m/s interval. The data and fits exhibit a clear speed dependence although each dissociation step is described by speed-*independent* anisotropy parameters. We find that the speed-*independent* anisotropy parameters are 1.2 ± 0.2 for the channel (1a) and on the basis of a comparison to the data. Likewise, we also determined the speed-*independent* anisotropy parameters for the channel (1b) to be 1.2 ± 0.4. The similarity of the anisotropy parameters for (1a) and (1b) suggests that the excited state leading to (1a) and (1b) are the same as suggested by Tanaka et al. It should be stressed that the primary dissociation prior to both secondary dissociation is (1a) from the branching ratios as discussed in this section. Top panel in Fig. 5 shows the derived β_4 of the $\mathrm{Cl}(^2\mathrm{P}_{3/2})$ fragments (circle) from the image data along with the Monte–Carlo forward-convolution fits using the anisotropy parameters for the primary dissociation of −1 (dash-dotted line), 0 (dashed line), and 1.2 (solid line) averaged over a 250-m/s interval. A positive β_4 is a result of a product of two positive β_2 (1.2, 1.8) for each dissociation step. Thus, the sign and the magnitude of the speed dependent β_4 are strong evidences for secondary photodissociation even if

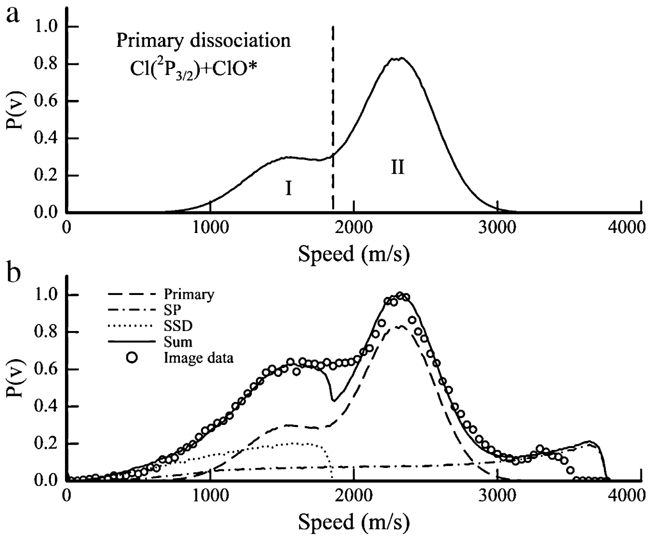

Fig. 4. (a) Derived speed distribution of $\mathrm{Cl}(^2\mathrm{P}_{3/2})$ arising from primary dissociation. Vertical line represents the three-body dissociation threshold. (b) Best-fit speed distribution of Cl fragments (solid line) from the primary dissociation (dashed line), secondary photodissociation (SP: dot and dashed line), spontaneous secondary dissociation (SSD: dotted line), and speed distribution from the image data (circle).

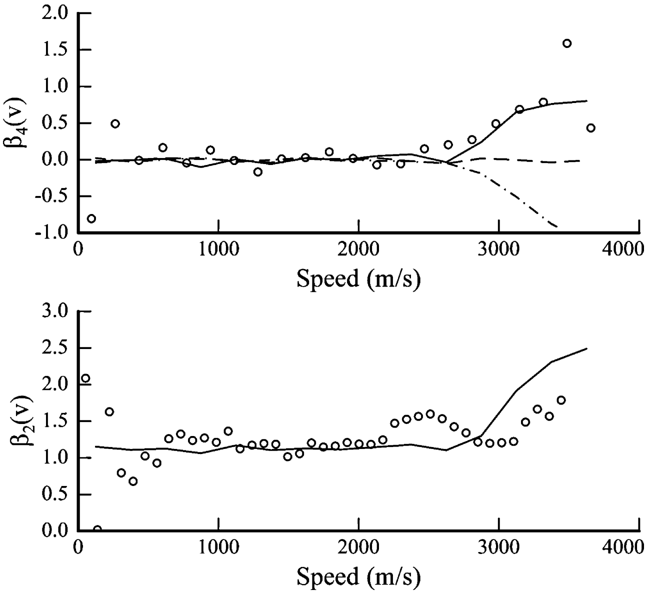

Fig. 5. Speed-dependent β_2 and β_4 for the $Cl(^2P_{3/2})$ fragments arising from the Cl_2O photodissociation at 235 nm along with the forward-convolutions fits.

its contribution to the whole image is small. In addition, β_4 provides another constraint for modeling secondary photodissociation to obtain accurate anisotropy parameters for each dissociation step.

4. Conclusions

We have investigated the photodissociation dynamics of expansion-cooled Cl_2O at 235 nm using velocity map ion imaging coupled with REMPI. We have observed speed-dependent β_2 and non-zero β_4 for both Cl atoms indicating that a fraction of nascent ClO undergoes secondary photodissociation. We have employed a Monte–Carlo forward-convolution fitting scheme for modeling the secondary photodissociation. On the basis of the forward-convolution fits, we find that branching ratios for $Cl(^2P_{3/2})$ + ClO and $Cl(^2P_{1/2})$ + ClO channels to be $0.97 \pm 0.02{:}0.03 \pm 0.02$ with anisotropy parameters of $\beta = 1.2 \pm 0.2$ and 1.2 ± 0.4, respectively. For $Cl(^2P_{3/2})$ + ClO channel, 28% of the parent molecule undergoes three-body dissociation whereas stable ClO are produced exclusively for $Cl(^2P_{1/2})$ + ClO channel.

Acknowledgements

This research was supported by the Duksung Women's University Research Grant 3000001300. The authors would like to thank Jennifer Putsche for technical assistance. The work by J.P. was supported by National Science Foundation REU Program (CHE-243829). S.W.N. would like to acknowledge support from the Robert A. Welch Foundation (Grant A-1402).

Appendix A. Supplementary data

Supplementary data associated with this article can be found, in the online version, at doi:10.1016/j.jphotochem.2011.04.036.

References

[1] M.J. Molina, F.S. Rowland, Nature 249 (1974) 840.
[2] S. Solomon, R.R. Garcia, F.S. Rowland, D.J. Wuebbles, Nature 321 (1986) 755.
[3] M. Schmeisser, Inorg. Synth. 9 (1967) 127.
[4] P. Zou, J. Park, B.A. Schmitz, T. Nguyen, S.W. North, J. Phys. Chem. A 106 (2002) 1004.
[5] C. Maul, K.-H. Gericke, Int. Rev. Phys. Chem. 16 (1997) 1.
[6] C. Maul, K.-H. Gericke, J. Phys. Chem. A 104 (2000) 2531.
[7] P. Zou, J. Shu, S.W. North, J. Photochem. Photobiol. A: Chem. 209 (2010) 56.
[8] L.T. Molina, M.J. Molina, J. Phys. Chem. 82 (1978) 2410.
[9] H.-D. Knauth, H. Alberti, H. Clausen, J. Phys. Chem. 83 (1979) 1604.
[10] J.B. Nee, J. Quant. Spectrosc. Radiat. Transf. 46 (1991) 55.
[11] S.L. Nickolaisen, C.E. Miller, S.P. Sander, M.R. Hand, I.H. Williams, J.S. Francisco, J. Chem. Phys. 104 (1996) 2857.
[12] C. Collaveri, G. Granucci, M. Persico, A. Toniolo, J. Chem. Phys. 115 (2001) 1251.
[13] C.M. Nelson, T.A. Moore, M. Okumura, T.K. Minton, J. Chem. Phys. 100 (1994) 8055.
[14] T.A. Moore, M. Okumura, T.K. Minton, J. Phys. Chem. 107 (1997) 3337.
[15] Y. Tanaka, M. Kawasaki, Y. Matsumi, H. Fujiwara, T. Ishiwata, L.J. Rogers, R.N. Dixon, M.N.R. Ashfold, J. Phys. Chem. 109 (1998) 1315.
[16] M. Roth, C. Maul, K.-H. Gericke, J. Phys. Chem. A 108 (2004) 7954.
[17] H. Kim, E.E. Greenwald, S.W. North, Chem. Phys. 364 (2009) 90.
[18] H. Kim, K.S. Dooley, E.R. Johnson, S.W. North, Rev. Sci. Instrum. 76 (2005) 124101.
[19] H. Kim, K.S. Dooley, E.R. Johnson, S.W. North, J. Chem. Phys. 124 (2006) 134304.
[20] S. Arepalli, N. Presser, D. Robie, R.J. Gordon, Chem. Phys. Lett. 117 (1985) 64.
[21] D.W. Chandler, P.L. Houston, J. Chem. Phys. 87 (1987) 1445.
[22] A.T. Eppink, D.H. Parker, Rev. Sci. Instrum. 68 (1997) 3447.
[23] B.-Y. Chang, R.C. Hoetzlein, J.A. Mueller, J.D. Geisler, P.L. Houston, Rev. Sci. Instrum. 69 (1998) 1665.
[24] V. Drinbinski, A. Ossadtchi, V.A. Mandelshtam, H. Reisler, Rev. Sci. Instrum. 73 (2002) 2634.
[25] J.L. Rogers, M.N.R. Ashfold, Y. Matsumi, M. Kawasaki, B.J. Whitaker, Chem. Phys. Lett. 258 (1996) 159.
[26] G.H. Cady, Inorg. Synth. 9 (1967) 127.
[27] M. Ahmed, D. Blunt, D. Chen, A.G. Suits, J. Chem. Phys. 106 (1997) 7617.
[28] J. Zhang, M. Dulligan, C. Wittig, J. Chem. Phys. 107 (1997) 1403.
[29] R.N. Zare, Mol. Photochem. 4 (1972) 1.
[30] H. Kim, J. Park, T.C. Niday, S.W. North, J. Chem. Phys. 123 (2005) 174303.